

## Article

# Enhancing Hardness and Wear Resistance of MgAl<sub>2</sub>O<sub>4</sub>/Fe-Based Laser Cladding Coatings by the Addition of CeO<sub>2</sub>

Liangxun Li <sup>1,2</sup>, Shaobai Sang <sup>1,2,\*</sup>, Tianbin Zhu <sup>1,2</sup>, Yawei Li <sup>1,2</sup> and Heng Wang <sup>1,2</sup>

<sup>1</sup> The State Key Laboratory of Refractories and Metallurgy, Wuhan University of Science and Technology, Wuhan 430081, China; 19107149721@163.com (L.L.); zhutianbin@wust.edu.cn (T.Z.); liyawei@wust.edu.cn (Y.L.); hengwang@wust.edu.cn (H.W.)

<sup>2</sup> National-Provincial Joint Engineering Research Center of High Temperature Materials and Lining Technology, Wuhan 430081, China

\* Correspondence: sangshaobai@126.com

**Abstract:** Laser cladding has unique advantages in improving the wear resistance of materials or workpiece surfaces. CeO<sub>2</sub> could play a role in promoting the flow of the molten pool and grain refinement during the laser cladding process, which is likely to further improve the wear resistance of the coating. In this work, CeO<sub>2</sub> was introduced into the MgAl<sub>2</sub>O<sub>4</sub>/Fe-based laser cladding coating on the surface of GCr15 steel. The effects of the CeO<sub>2</sub> content on the phase composition, microstructure, hardness, and wear resistance of the coatings were also systematically investigated. The results showed that the addition of CeO<sub>2</sub> enhanced the continuity of the coating and reduced the size of the MgAl<sub>2</sub>O<sub>4</sub> particles, which was associated with the addition of CeO<sub>2</sub>'s intensification of the melt pool flow. The metal grain size reduced and then increased as the CeO<sub>2</sub> content increased, whereas the hardness and wear resistance of the MgAl<sub>2</sub>O<sub>4</sub>/Fe-based coatings increased and then decreased. Compared with the MgAl<sub>2</sub>O<sub>4</sub>/Fe-based coating without CeO<sub>2</sub>, the hardness of the MgAl<sub>2</sub>O<sub>4</sub>/Fe-based coating with 1.0 wt% CeO<sub>2</sub> increased by 10% and the wear rate decreased by 40%, which was attributed to the metal grain refinement and particle dispersion strengthening.

**Keywords:** laser cladding; Fe-based coating; CeO<sub>2</sub>; hardness; wear resistance



**Citation:** Li, L.; Sang, S.; Zhu, T.; Li, Y.; Wang, H. Enhancing Hardness and Wear Resistance of MgAl<sub>2</sub>O<sub>4</sub>/Fe-Based Laser Cladding Coatings by the Addition of CeO<sub>2</sub>. *Coatings* **2024**, *14*, 550. <https://doi.org/10.3390/coatings14050550>

Academic Editor: Angela De Bonis

Received: 7 April 2024

Revised: 26 April 2024

Accepted: 26 April 2024

Published: 28 April 2024



**Copyright:** © 2024 by the authors. Licensee MDPI, Basel, Switzerland. This article is an open access article distributed under the terms and conditions of the Creative Commons Attribution (CC BY) license (<https://creativecommons.org/licenses/by/4.0/>).

## 1. Introduction

Surface coating technology, as a technique to improve the surface properties of materials without changing the primary material, has been widely researched due to its ability to extend the service life of materials [1–3]. In the industrial field, the high frictional wear of workpieces results from the poor tribological properties of materials or workpiece surfaces, such as steel rollers. Therefore, the preparation of wear-resistant coatings on the surface of workpieces has become a hot research direction. In recent years, laser cladding has become the focus of research in the field of material surface strengthening due to its unique advantages in improving the wear resistance of materials or workpiece surfaces [4,5].

Fe-based, Co-based, and Ni-based alloys are commonly used as raw materials for laser cladding. Wu [6] and Guo [7] et al. found that the high hardness and wear resistance of the alloy coatings result from the microstructure refinement and carbide precipitation caused by the high-energy laser. With the development of industry, alloy coatings no longer meet the requirements of complex working conditions. Researchers began looking for ways to improve the hardness and wear resistance of laser-clad alloy coatings. Duan et al. [8] introduced nano-Al<sub>2</sub>O<sub>3</sub> into an Fe-based laser cladding coating on the surface of 316L steel. The formation of dispersive distributions of Al<sub>2</sub>O<sub>3</sub> and Fe<sub>3</sub>Al inhibited the grain growth, thereby improving the hardness and wear resistance of the Fe-based coating. Liu et al. [9] introduced WC into a Ni-based laser cladding coating on the surface of 45 steel. The unmolten WC particles provided nucleation points and hindered the grain growth. The refinement of the microstructure improved the hardness and wear resistance

of Ni50 coatings. Therefore, ceramic-reinforced metal matrix composite (CRMMC) coatings have been widely researched for their high designability, high hardness, and high wear resistance [10,11]. However, when large amounts of ceramic phase were added to the alloy coating, defects such as coating discontinuities occurred due to differences in the physical properties such as the coefficient of thermal expansion and wettability between the ceramic phase and the alloy [12].

In recent years, researchers have found that the addition of rare-earth oxides could effectively reduce the generation of defects and further improve the performance of coatings [13,14]. CeO<sub>2</sub>, as a widely used rare-earth material, has excellent properties such as high chemical activity, high melting point, high hardness, etc., [15,16]. Liu et al. [17] found that the addition of CeO<sub>2</sub> could promote the flow of molten pools. With the increase in CeO<sub>2</sub> mass fraction, the molten pool flow mode changed, and the flow rate first increased and then decreased. When CeO<sub>2</sub> was appropriate, the melt flow drove the crack-sensitive phases such as gases and impurities up to the coating surface, and promoted the homogeneity of the elements, according to Murmu et al. [18]. In addition to promoting the melt pool flow, CeO<sub>2</sub> can also play an important role in grain refinement. According to Wei et al. [19], nano-CeO<sub>2</sub> reduced the critical nucleation energy in coatings and served as a non-homogeneous phase nucleation site, which promoted grain nucleation. And then it inhibited grain development through the polycrystalline boundaries generated by grain nucleation. Zhao [20] and Quazi [21] et al. found that rare-earth elements accumulated and pinned to the grain boundaries, dragging and hindering the movement of the grain boundaries during the grain growth. Therefore, the addition of CeO<sub>2</sub> to CRMMC coatings could effectively repair coating defects and further improve the coating wear resistance.

At present, there are fewer reports on MgAl<sub>2</sub>O<sub>4</sub> as a reinforced phase being added into the alloy in a large proportion to prepare MgAl<sub>2</sub>O<sub>4</sub>/Fe-based laser cladding coatings. Based on this, CeO<sub>2</sub> was used to accelerate the flow of the molten pool and promote the uniform dispersion of ceramics to prepare CeO<sub>2</sub>/MgAl<sub>2</sub>O<sub>4</sub>-reinforced Fe-based laser cladding coatings with high hardness, high wear resistance, and low cost. Moreover, some small steel rollers were made of GCr15; as a result, GCr15 was selected as the substrate in this work. Specifically, the effects of the CeO<sub>2</sub> content on the morphology and microstructure of the MgAl<sub>2</sub>O<sub>4</sub>/Fe-based coatings were explored; also, the enhancement mechanism of the CeO<sub>2</sub> addition on the hardness and wear resistance of the MgAl<sub>2</sub>O<sub>4</sub>/Fe-based coatings was discussed in detail.

## 2. Materials and Methods

GCr15 steel was used as the substrate material with a size of 60 mm × 40 mm × 10 mm, and its chemical compositions were C 0.95–1.05 wt%, Mn 0.25–0.45 wt%, Cr 1.40–1.65 wt%, Si 0.15–0.35 wt%, Mo ≤ 0.10 wt%, S ≤ 0.025 wt%, P ≤ 0.025 wt%, Ni ≤ 0.30 wt%, Cu ≤ 0.25 wt%, Ni + Cu ≤ 0.50 wt%, and Fe balance.

Fe-based alloy particles (C 0.07 wt%, Cr 17.5 wt%, Si 0.8 wt%, Ni 7.0 wt%, and Fe balance, 100 μm, Tianjin Casting Gold Technology Development Co., Ltd., Tianjin, China), MgAl<sub>2</sub>O<sub>4</sub> particles (Al<sub>2</sub>O<sub>3</sub> 77.5 wt%, MgO 21.5 wt%, CaO 0.40 wt%, and SiO<sub>2</sub> 0.35 wt%, 100–200 μm, Jiangsu Jingxin New Material Co., Ltd., Yangzhou, China), CeO<sub>2</sub> (99.99% analytically pure, Shanghai Macklin Biochemical Technology Co., Ltd., Shanghai, China), and sodium carboxymethyl cellulose (analytically pure, Shanghai Macklin Biochemical Technology Co., Ltd.) were used as raw materials. The scanning electron microscope (SEM) morphology of the main raw materials is shown in Figure 1.

The substrate was polished with sandpaper of 400#, 600#, and 800# for 5 min in turn before the experiment, then ultrasonically cleaned with ethanol to remove surface oxidation and oil. Based on the results of previous optimization experiments, Fe-based alloy powder and MgAl<sub>2</sub>O<sub>4</sub> particles were weighed at 70 wt% and 30 wt%, to which 0%, 0.5 wt%, 1.0 wt%, and 1.5 wt% of CeO<sub>2</sub> powder were added, respectively. Considering the particle sedimentation of Fe-based alloy powder in the slurry, sodium carboxymethyl cellulose solution (sodium carboxymethyl cellulose: deionized water = 0.6:100) was added

to the composite powders to prepare the slurry. The slurry was mixed by a dispersion mixer (SFJ-400, Shanghai Xiandai Environment Engineering Technique Co., Ltd., Shanghai, China) at a speed of 1000 rpm for 30 min. The mixed slurry was coated on the substrate, and the samples were placed in an oven at 120 °C for 3 h. The samples with a solid preset coating were prepared after drying. Based on pre-optimization experiments and considering the dilution rate and continuity of the coatings, the preset coating thickness was 1 mm. A high-power semiconductor laser (model: C4000X; maximum output power: 4000 W; laser beam wavelength:  $1080 \pm 5$  nm) was used to prepare the laser cladding coating, as shown in Figure 2. According to the results of previous optimization experiments, the laser cladding process parameters used in this experiment were as follows: laser power of 1800 W, scan speed of 4 mm/s, and spot diameter of 5 mm. The samples with 0, 0.5 wt%, 1.0 wt%, and 1.5 wt% CeO<sub>2</sub> powder were labeled as C0, C0.5, C1.0, and C1.5, respectively.

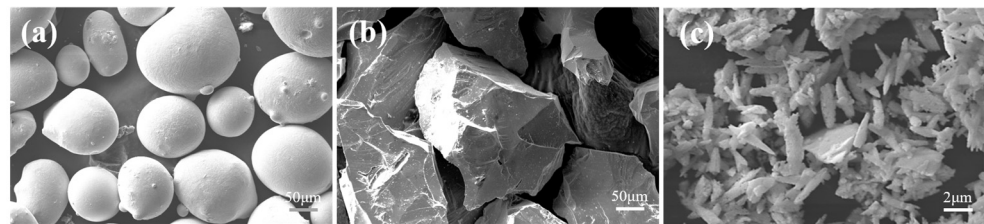


**Figure 1.** SEM morphology of raw materials: (a) Fe-based alloy; (b) MgAl<sub>2</sub>O<sub>4</sub>; (c) CeO<sub>2</sub>.

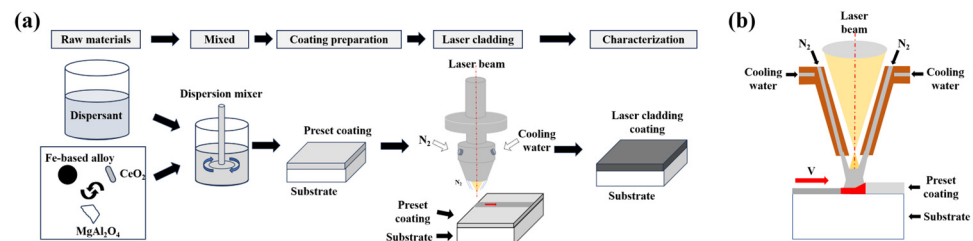


**Figure 2.** (a) Experimental procedure; (b) schematic diagram of laser cladding.

Metallographic samples were prepared and then polished. The samples were etched by aqua regia (HCl: HNO<sub>3</sub> = 3:1) for 5–7 s, then rinsed with water and ethanol, dried and characterized.

The macro-morphology of the samples was observed using an optical microscope (OM, Carl Zeiss AG, Oberkochen, Germany). The microstructure and elemental distribution of the samples were obtained using a scanning electron microscope (SEM, JSM-6610, JEOL Co., Ltd., Tokyo, Japan) and its equipped energy disperse spectroscopy (EDS). The phase composition of the samples was characterized by an X-ray diffractometer (XRD, X' Pert Pro, Malvern Panalytical, Worcester, UK) under the following conditions: Cu target, Kal-ray, tube voltage of 30 kV, tube current of 30 mA, scanning range of 10–90°.

The microhardness of the laser cladding coating was tested using a Vickers hardness tester (HV-50A, Laizhou Huayin Testing Instruments Co., Ltd., Yantai, China) from the surface to the interior at intervals of 0.2 mm with a load of 10 kg and a duration of 15 s. To minimize inaccuracy, three distinct points were evaluated at the same distance from the surface. The average value was then derived to represent the microhardness.

The reciprocating dry sliding wear test was performed using the comprehensive material surface properties tester (HRS-2M, Lanzhou Zhongke Kaihua Technology Development Co., Ltd., Lanzhou, China). A Si<sub>3</sub>N<sub>4</sub> ball with a diameter of 6 mm was chosen as the grinding ball, and the test parameters were as follows: load of 30 N, time of 20 min, sliding distance of 5 mm, and speed of 5 m/min. A displacement sensing probe took measure-

ments of the wear marks' two-dimensional cross-sectional profile. Equation (1) was used to calculate the precise wear rate [22].

$$K_v = \frac{\Delta V}{F_N \cdot S} \left( \text{mm}^3 \cdot \text{N}^{-1} \cdot \text{m}^{-1} \right) \quad (1)$$

In Equation (1),  $F_N$  is the load applied to the sample by the grinding ball (N),  $S$  is the total sliding distance of the grinding ball (m), and  $\Delta V$  is the volume loss after the wear test ( $\text{mm}^3$ ). The  $\Delta V$  of the samples can be determined by using Equation (2).

$$\Delta V = A \cdot L \left( \text{mm}^3 \right) \quad (2)$$

In Equation (2),  $A$  is the average area of the two-dimensional cross-section of the wear marks ( $\text{mm}^2$ ) and  $L$  is the length of the wear marks (mm).

### 3. Results

#### 3.1. Phase Compositions

As for the sample C0,  $\alpha$ -Fe,  $\text{CFe}_{15.1}$ ,  $(\text{Fe, Cr})_7\text{C}_3$ , and  $\text{Fe}_3\text{Al}$  phases were detected, as shown in Figure 3. The molten decomposition of some of the  $\text{MgAl}_2\text{O}_4$  under a high-energy laser beam produced  $\text{Al}_2\text{O}_3$ , which then interacted with the surrounding Fe to generate  $\text{Fe}_3\text{Al}$ . The intensity of the diffraction peak of the  $\text{CFe}_{15.1}$  phase was reduced in the samples with  $\text{CeO}_2$  added compared to the sample C0. The C atoms precipitated during the cooling process of  $\text{CFe}_{15.1}$  were reacted with elements such as Fe and Cr, which ultimately contributed to the enhancement in the intensity of the diffraction peaks of the  $\alpha$ -Fe and  $(\text{Fe, Cr})_7\text{C}_3$  phases [23]. When the content of  $\text{CeO}_2$  was 1.5 wt%, a new phase appeared in the coating. It could be seen by comparing the standard PDF card that the new phase was  $\text{CeAl}_2$ . Meanwhile, the generation of the new phase of  $\text{CeAl}_2$  might be due to the reaction of the partially decomposed  $\text{Al}_2\text{O}_3$  with the highly chemically active Ce atoms [8,24]. Moreover, it was difficult to detect  $\text{CeO}_2$  diffraction peaks in the samples with  $\text{CeO}_2$ . On the one hand, this was related to the small amount of  $\text{CeO}_2$  added. On the other hand, it was due to the reaction of  $\text{CeO}_2$  with the rest of the elements to generate new phases.

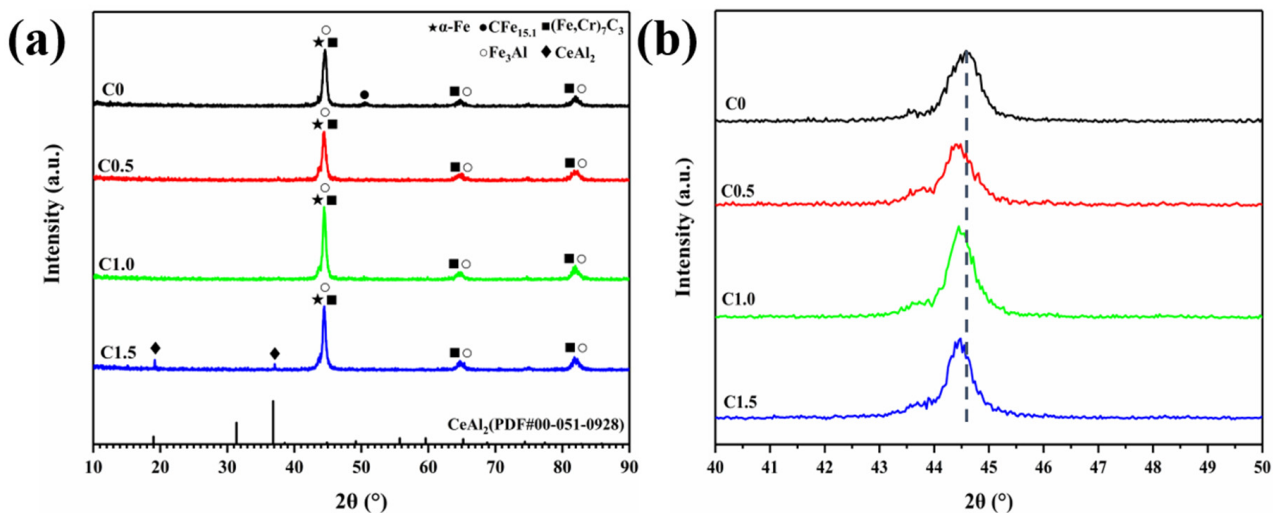


**Figure 3.** (a) XRD patterns of coatings with different  $\text{CeO}_2$  content; (b) partial enlarged view of the XRD pattern.

#### 3.2. Microstructure

From Figure 4a–d, with the increase in the  $\text{CeO}_2$  content, the surface of coatings with 0.5 wt% and 1.0 wt%  $\text{CeO}_2$  became flat rather than rugged. This was because the

addition of  $\text{CeO}_2$  increased the laser energy absorption of the material and promoted the flow of the molten pool, thus making the coating flatter. It was similar to the results of references [17,25,26]. Meanwhile, the high chemical activity of  $\text{CeO}_2$  reduced the surface tension of the molten alloy, which caused the molten alloy to flow toward the center of the molten pool and to form a wedge-shaped cladding layer [17]. However, the addition of excess  $\text{CeO}_2$  interrupted the coating with 1.5 wt%  $\text{CeO}_2$ .

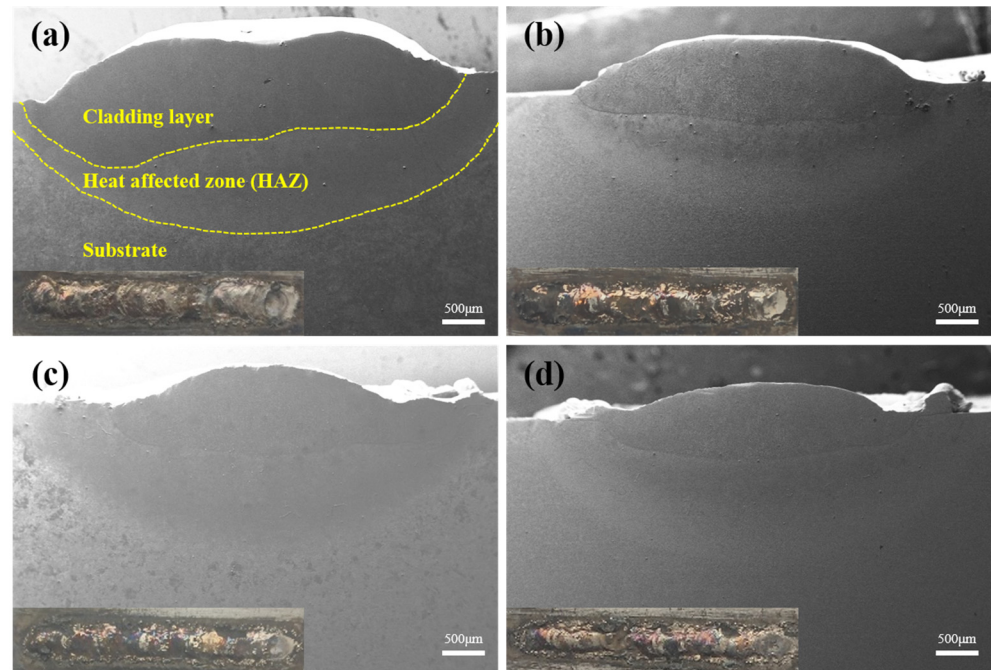


**Figure 4.** Cross-sectional morphology of different samples: (a) C0; (b) C0.5; (c) C1.0; (d) C1.5.

As shown in Figure 5(a<sub>1</sub>–a<sub>3</sub>), the coating could be divided into three regions based on the metal grain growth: top, middle, and bottom. The metal grain morphology in different regions of the coating mainly depended on the temperature gradient  $G$  and solidification rate  $R$  [27,28]. The bottom of the coating first formed columnar crystals by epitaxial growth in the direction of the temperature gradient through non-uniform nucleation. Meanwhile, the low solidification rate at the bottom of the coating allowed the metal grains to fully develop to form cellular crystals. Therefore, columnar crystals mainly dominated at the bottom of the coating. The temperature gradient  $G$  at the top and middle of the coating decreased, the solidification rate  $R$  increased, and the value of  $G/R$  was small. The metal grains were refined and did not grow selectively but grew and developed in multiple directions to form equiaxial crystals and dendritic crystals. Therefore, equiaxial crystals and dendrites dominated at the top and middle of the coating.

Comparing with Figure 5(a<sub>2</sub>–d<sub>2</sub>), it was shown that with the increase in the  $\text{CeO}_2$  content, the metal grain size decreased first and then increased. This was because the addition of  $\text{CeO}_2$  improved the latent heat of melting, increased the solid-phase temperature of the molten pool, and reduced the solidification temperature range and solidification time, thus shortening the metal grain development time; meanwhile, the high melting point of  $\text{CeO}_2$  made some of the unmolten  $\text{CeO}_2$  act as nucleation sites to promote the non-uniform nucleation of metal grains. The highly chemically active  $\text{CeO}_2$  was generally located at the grain boundaries and reduced the critical nucleation energy, which promoted the nucleation of metal grains and hindered the metal grain growth [19,29,30]. When the  $\text{CeO}_2$  content was 1.0 wt%, the metal grain size of the sample C1.0 was the smallest. However, when the  $\text{CeO}_2$  content was 1.5 wt%, excess  $\text{CeO}_2$  was aggregated, reducing the effect of rare earths on the metal grain refinement [31].

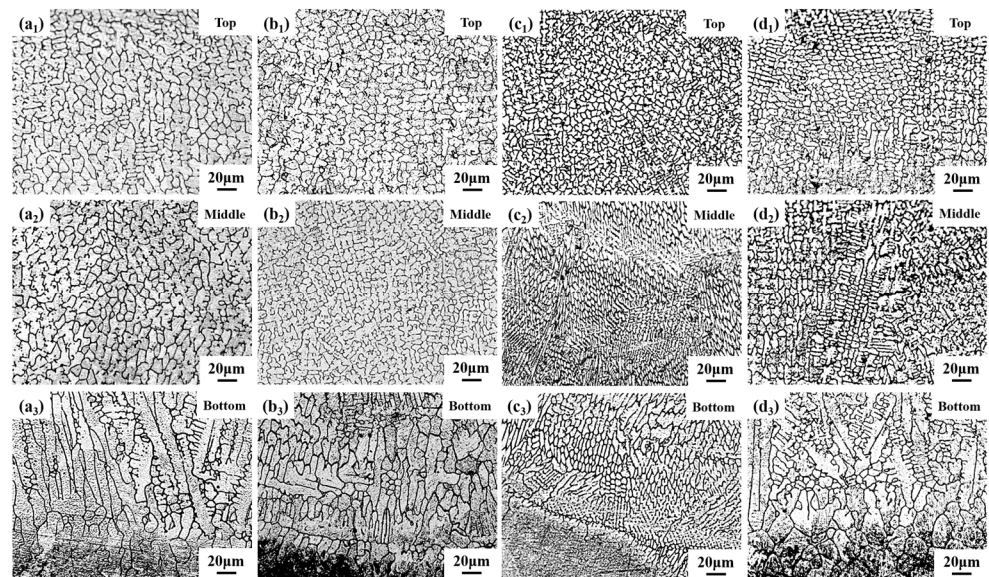


**Figure 5.** Optical microscope morphology of the cross-section of the samples: (a<sub>1</sub>–a<sub>3</sub>) C0; (b<sub>1</sub>–b<sub>3</sub>) C0.5; (c<sub>1</sub>–c<sub>3</sub>) C1.0; (d<sub>1</sub>–d<sub>3</sub>) C1.5.

When the CeO<sub>2</sub> content increased, it was demonstrated that equiaxial crystals increased and columnar crystals decreased in comparison to Figure 5(a<sub>3</sub>–d<sub>3</sub>). However, the number of columnar crystals increased again when the CeO<sub>2</sub> content was 1.5 wt%. It was worth noting that the addition of CeO<sub>2</sub> induced competition between native columnar crystals and non-uniformly nucleated equiaxial crystals. With the increase in the CeO<sub>2</sub> content, the columnar crystals had an obvious tendency to transform into the equiaxed crystals [17]. However, when the CeO<sub>2</sub> content was excessive, the Ce atoms reacted with the rest of the elements to form intermetallic compounds, which weakened the metal grain refinement effect. In addition, the ability of CeO<sub>2</sub> to inhibit the growth of columnar crystals was weakened, resulting in the columnar crystals no longer being transformed into equiaxed crystals.

With the increase in the CeO<sub>2</sub> content, the particle size of ceramic-reinforced phases such as MgAl<sub>2</sub>O<sub>4</sub> decreased continuously (Figure 6a–d), and the particles gradually migrated to the grain boundaries (some of the ceramic particles were marked by yellow dashed lines). On the one hand, the addition of CeO<sub>2</sub> enhanced the molten pool fluidity. The melt eroded the ceramic particles and reduced the particle size. The refinement of the ceramic particles enhanced the particle dispersion-strengthening effect. On the other hand, the flow of the melt pool would drive the ceramic particles toward the high-activity sites where CeO<sub>2</sub> was located, and the ceramic particles pinned at the grain boundaries and refined the metal grains [32,33]. The metal grain size decreased first and then increased with the increase in the CeO<sub>2</sub> content, as shown in Figure 6e–h. The effect of the CeO<sub>2</sub> content on the coating structure is shown in Figure 7. In addition, some of the MgAl<sub>2</sub>O<sub>4</sub> decomposed under low oxygen partial pressure conditions. The main composition of the ceramic particles was Al<sub>2</sub>O<sub>3</sub>, which was similar to the findings of Yan et al. [34,35]. The elemental distribution of the ceramic particles is shown in Table 1.

**Table 1.** EDS elemental analysis of different regions of the coatings.

Region	Cr (wt%)	Al (wt%)	Mg (wt%)	Ce (wt%)	C (wt%)	O (wt%)	Ni (wt%)	Fe (wt%)
Spot 1	0.86	53.47	0.02		6.63	36.59	0.52	1.91
Spot 2	6.57	0.21			3.62	0.76	2.58	86.26
Spot 3	11.74	0.19	0.02		2.05	1.23	1.58	83.19
Spot 4	24.39	0.59	0.02		5.00	2.23	1.25	66.52
Spot 5	19.69	4.63	0.13	2.19	8.11	9.07	2.45	53.73

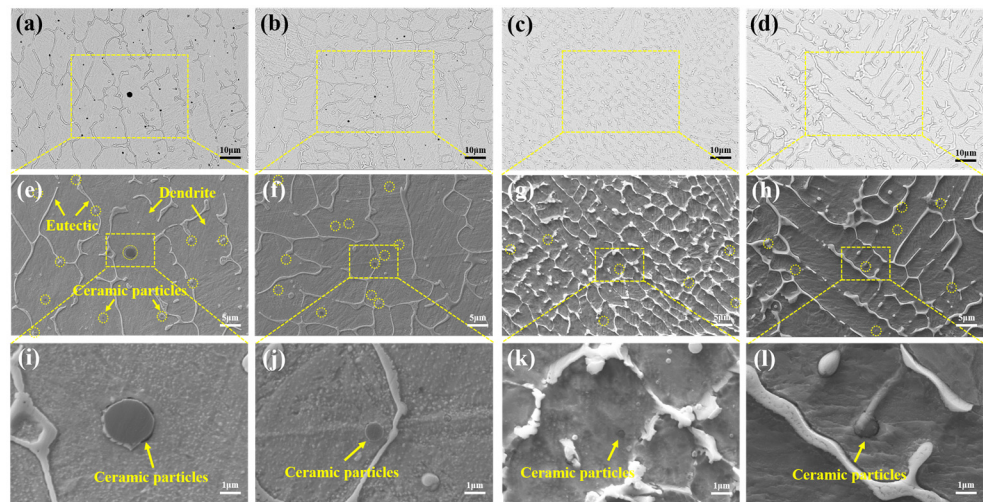


**Figure 6.** SEM and BSE images of cross-sections of different samples: (a,e,i) C0; (b,f,j) C0.5; (c,g,k) C1.0; (d,h,l) C1.5.

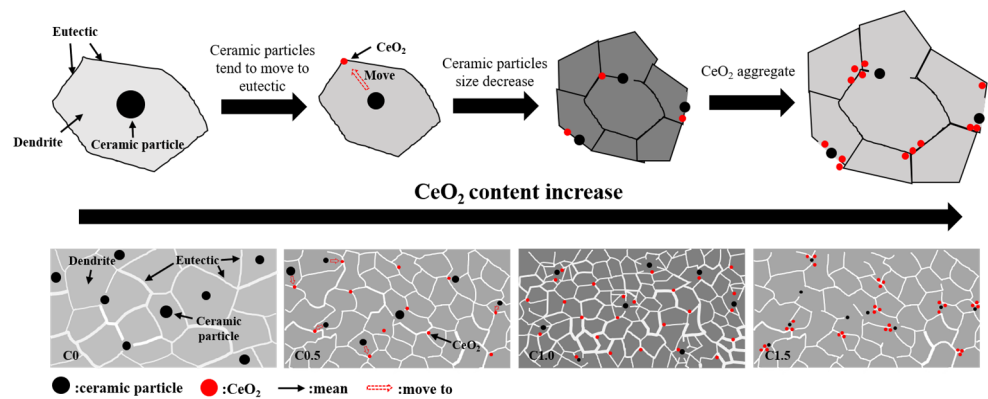


**Figure 7.** The effect of  $\text{CeO}_2$  content on the coating structure and ceramic particles.

As shown in Figure 8(a<sub>1</sub>–d<sub>1</sub>) and Table 1 (The star symbols in Figure 8 are the EDS element scanning regions), the Cr content in the C0 coating increased significantly from 6.57 wt% in the dendrite structure to 11.74 wt% in the eutectic structure. And with the addition of  $\text{CeO}_2$ , the Cr element in the eutectic structure increased again, from 11.74 wt% to 24.39 wt%. Since  $\text{CeO}_2$  was highly chemically active, the added  $\text{CeO}_2$  tended to aggregate and be pinned at the grain boundaries to maintain the lowest free energy in the system. Meanwhile,  $\text{CeO}_2$  enhanced the enrichment effect of the Cr element in the eutectic structure, increasing the content of Cr elements there [21,25]. In addition, some  $\text{CeO}_2$  could be found to accumulate spontaneously at the grain boundaries, as shown in Figures 8(d<sub>1</sub>) and 9.

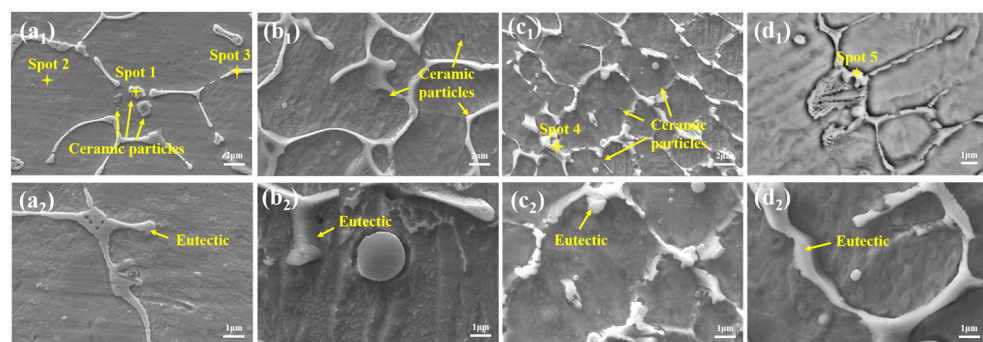


**Figure 8.** SEM morphology and BES images of cross-sections of different samples: (a<sub>1</sub>,a<sub>2</sub>) C0; (b<sub>1</sub>,b<sub>2</sub>) C0.5; (c<sub>1</sub>,c<sub>2</sub>) C1.0; (d<sub>1</sub>,d<sub>2</sub>) C1.5.

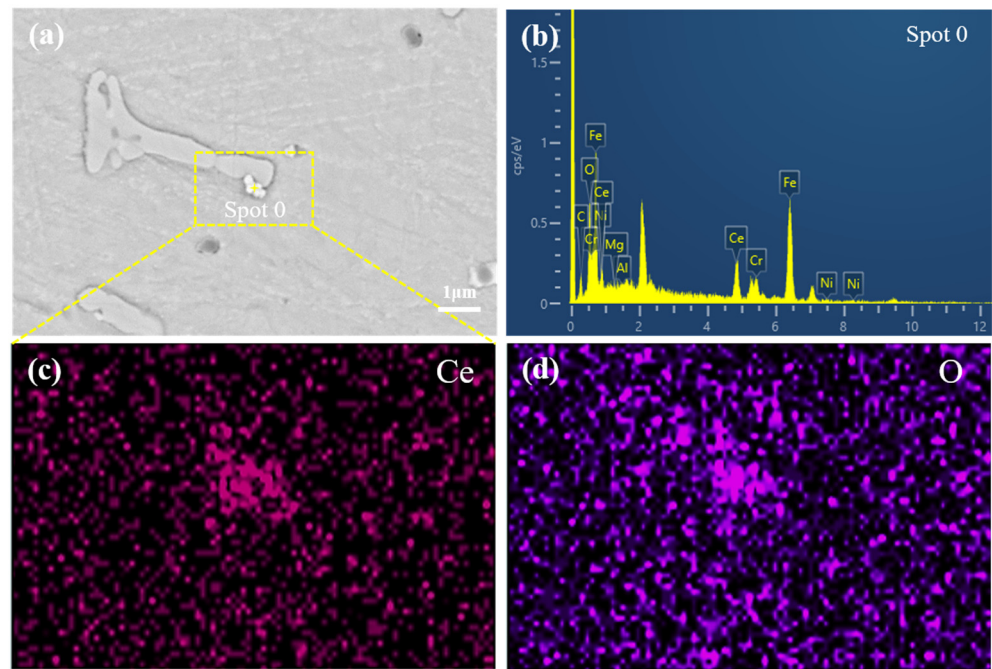


**Figure 9.** Elemental distribution of CeO<sub>2</sub> particles in sample C1.5: (a) BSE images of sample C1.5; (b) the peak map of the elemental distribution of CeO<sub>2</sub> particles; (c) map-scanning elemental distribution of Ce in CeO<sub>2</sub> particles; (d) map-scanning elemental distribution of O in CeO<sub>2</sub> particles.

There was a height difference between the eutectic structure and the dendritic structure under the aqua regia etching condition, as shown in Figure 8(a<sub>2</sub>–d<sub>2</sub>). This was because the eutectic structure with a higher Cr content exhibited stronger corrosion resistance than the surrounding dendritic structure. With the addition of CeO<sub>2</sub>, the Cr content in the eutectic structure of samples C1.0 and C1.5 increased, as shown in Table 1. The height difference between the eutectic structure and the dendritic structure in samples C1.0 and C1.5 further increased. Indirectly, it proved the enhancement of CeO<sub>2</sub> on the enrichment of Cr elements.

### 3.3. Hardness

Figure 10a shows the Vickers hardness distribution profiles of cross-sections at every 0.2 mm from the surface. Figure 10b shows the average Vickers hardness of the coating within 0.8 mm from the surface.

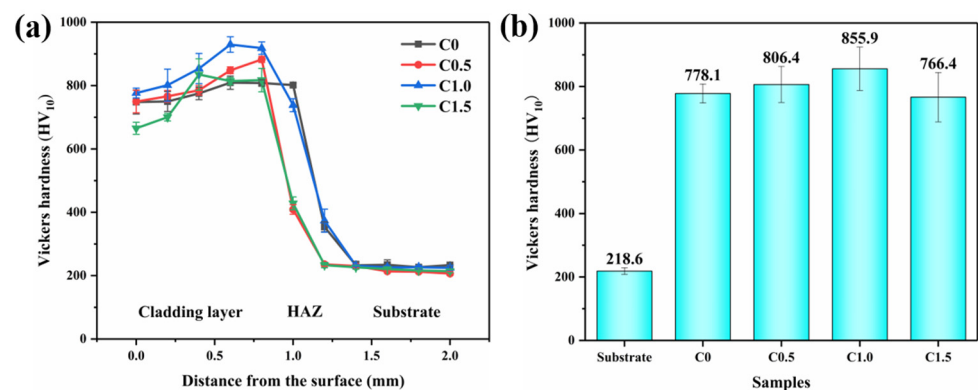


**Figure 10.** (a) Cross-sectional Vickers hardness distribution of different samples; (b) the average Vickers hardness of the coating within 0.8 mm from the surface.

According to Figure 10a, taking the sample C0 as an example, the maximum hardness of the sample C0 was not at the surface. It was due to the high-energy laser beam causing

damage to the surface of the coating. Therefore, there were differences in the hardness at different locations of the sample C0, and the average hardness of the sample C0 needed to be calculated for analysis.

In Figure 10b, compared to the substrate (219 HV<sub>10</sub>), the average hardness of the sample C0 was 778 HV<sub>10</sub>, which was 3.6 times higher than that of the substrate. The increase in the hardness of the sample C0 was related to the ceramic-reinforced phases like MgAl<sub>2</sub>O<sub>4</sub>. On this basis, the addition of CeO<sub>2</sub> further improved the hardness of the sample C0.

The average hardness of the coatings showed an increasing and then decreasing trend with the increase in the CeO<sub>2</sub> content. The highest average hardness (856 HV<sub>10</sub>) was observed for the sample C1.0, which was 3.9 times higher than that of the substrate, with an increase of 10% compared to the sample C0. The increase in the coating hardness was related to the metal grain refinement and particle dispersion strengthening due to the addition of CeO<sub>2</sub>. On the one hand, CeO<sub>2</sub> refined the metal grains and induced columnar crystals to transition into equiaxed crystals. The equiaxed crystals' high symmetry and the refined metal grains' polycrystalline boundaries successfully resisted the dislocation slip under pressure. On the other hand, the refinement of the ceramic particles further enhanced the particle dispersion-strengthening effect.

However, the hardness of the sample C1.5 decreased instead when the CeO<sub>2</sub> content was excessive. The excess CeO<sub>2</sub> would aggregate, weakening the metal grain refinement effect of CeO<sub>2</sub>, thus decreasing the hardness of the sample C1.5.

### 3.4. Wear Behavior

Figure 11a shows the coefficients of friction for different samples. For the stability of the experiment, the average value of the coefficient of friction was calculated using the average value of the stable wear stage, after 5 min, as shown in Figure 11b.

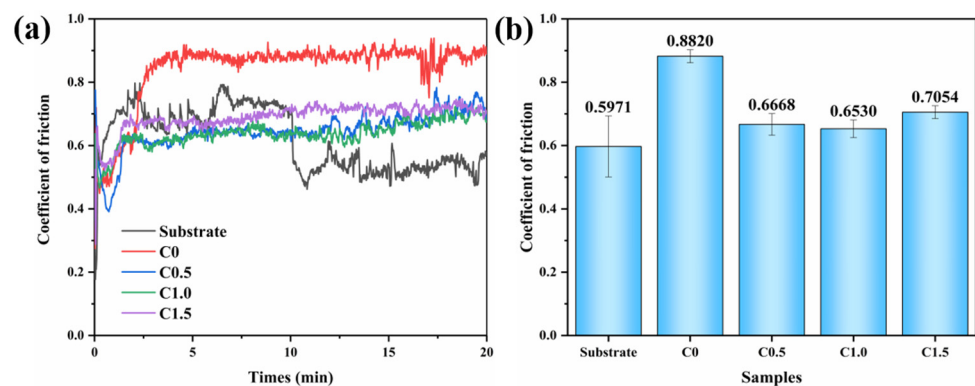


**Figure 11.** (a) Coefficient of friction of different samples; (b) average value of coefficient of friction.

The coefficient of friction of the substrate decreased abruptly at 10 min of reciprocal friction, as shown in Figure 11a. The continuous oxide film appearing in the substrate during friction acted as a lubrication phase to reduce the friction coefficient. Compared with the substrate, the friction coefficients of samples C0, C0.5, C1.0, and C1.5 were more stable with less fluctuation, which was related to the increase in the hardness of the coating. When the hardness increased, the coating could effectively resist the pressure in and shear of the grinding ball during the friction process, thus enhancing the stability of the friction coefficient.

As shown in Figure 11b, the average coefficient of friction decreased and then increased with the increase in the CeO<sub>2</sub> content. Firstly, the added CeO<sub>2</sub> enhanced the hardness of the coating by metal grain refinement and particle dispersion strengthening. And with the further increase in the CeO<sub>2</sub> content, the resistance effect of the coating to grinding was improved, thus reducing the coefficient of friction. However, when the CeO<sub>2</sub> content was

too high, the coefficient of friction of the sample C1.5 increased instead, which was related to the reduction in the hardness.

The two-dimensional cross-sectional profiles and wear rates for different samples are shown in Figure 12. The abrasion depth of the substrate and sample C0 was large and the profile was relatively flat, while the abrasion depth of samples C0.5 and C1.0 was significantly reduced, and the profile was more rugged. It proved that the addition of CeO<sub>2</sub> increased the hardness of the coating and blocked the sliding of the grinding ball. Meanwhile, the cross-sectional areas of the abrasion marks were substrate, C0, C0.5, C1.5, and C1.0, from the largest to the smallest, as shown in Figure 12a. Equations (1) and (2) showed that the smaller the cross-sectional area, the smaller the wear rate. Therefore, the sample C0 had the lowest wear rate of  $3.84 \times 10^{-6} \text{ mm}^3 \cdot \text{N}^{-1} \cdot \text{m}^{-1}$ , which was decreased by 40% and 70%, respectively, compared to those of the sample C0 and the substrate. However, the wear rate of the sample C1.5 decreased, in contrast to the trend of the coating hardness in Figure 10b. It was essentially compatible with Archard's law [36].

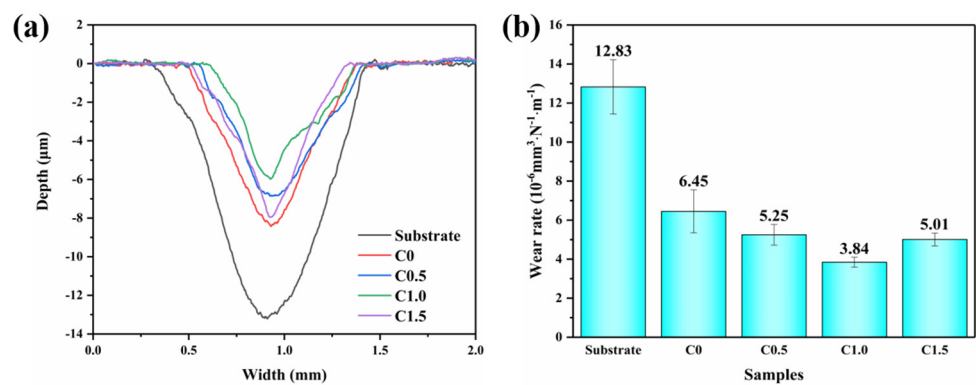


Figure 12. (a) Two-dimensional cross-sectional abrasion profiles of different samples; (b) wear rates of different samples.

As shown in the morphology of the wear marks in Figure 13(a<sub>1</sub>–d<sub>1</sub>), with the increase in the CeO<sub>2</sub> content, the content of the adhesive phase in the wear marks decreased and the number of grooves increased. However, the content of the adhesive phase on the C1.5 wear marks increased instead, which was related to the decrease in the coating hardness.

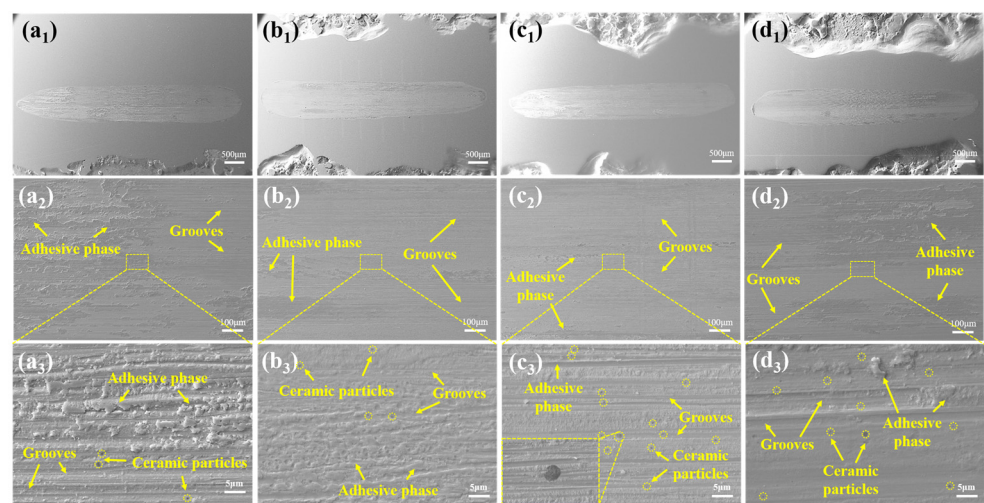


Figure 13. SEM morphology of different samples with wear marks: (a<sub>1</sub>–a<sub>3</sub>) C0; (b<sub>1</sub>–b<sub>3</sub>) C0.5; (c<sub>1</sub>–c<sub>3</sub>) C1.0; (d<sub>1</sub>–d<sub>3</sub>) C1.5.

As shown in Figure 13(a<sub>3</sub>–d<sub>3</sub>), the ceramic particles were present in all samples (some of which were marked by yellow dashed lines). The improvement in the ceramic particles

on the wear resistance of the coating was mainly reflected in two ways. On the one hand, it increased the hardness of the coating to resist the pressure and shear force of the grinding ball. On the other hand, increasing the number of abrasive particles reduced the contact area between the grinding balls and the coating.

Micro-welding between the friction pairs occurred during the friction process. The micro-welded areas were fractured and spalled due to the relative motion, and the spalled material was transferred by the grinding balls to form an adhesive phase. Some adhesive phases were present on the surface of the sample C0 wear marks, as shown in Figure 13(a<sub>3</sub>). Meanwhile, numerous deep and long grooves appeared on the sample C0 wear marks under the micro-cutting effect of the grinding ball [37]. It was indicated that the sample C0 hardness was relatively low and could not effectively resist the cutting of the grinding balls and the indentation shear of the abrasive particles. Therefore, serious adhesive and abrasive wear existed in sample C0.

With the increase in the CeO<sub>2</sub> content, the content of the adhesive phase in the samples C0.5 and C1.0 decreased, and the number and depth of grooves decreased, which were related to the increase in the hardness of the coating and the resistance of the hard ceramic particles to the movement of the grinding ball (some of the ceramic particles were marked by yellow dashed lines). The wear mechanism of the samples C0.5 and C1.0 was more inclined toward abrasive wear. However, the content of the adhesive phase of the sample C1.5 wear marks increased instead, the groove depth increased, and the adhesive phase was concentrated at the grooves. Combined with Figure 10b, it was evident that the excess CeO<sub>2</sub> decreased the hardness of the sample C1.5. As a result, the ability of the sample C1.5 to resist the indentation and shear of the grinding ball was weakened, and the contact area between the grinding ball and the coating was increased. Therefore, the wear mechanism of the sample C1.5 was more inclined toward adhesive wear with some abrasive wear.

#### 4. Conclusions

In this work, MgAl<sub>2</sub>O<sub>4</sub>/Fe-based coatings with different CeO<sub>2</sub> contents were prepared on the surface of GCr15 steel by laser cladding. The influence of the CeO<sub>2</sub> content on the phase compositions, microstructure, and wear resistance of the coatings were systematically investigated. The main conclusions were as follows:

- (1) With the introduction of CeO<sub>2</sub>, the main phases ( $\alpha$ -Fe, CFe<sub>15.1</sub>, (Fe, Cr)<sub>7</sub>C<sub>3</sub>, and Fe<sub>3</sub>Al phases) of the MgAl<sub>2</sub>O<sub>4</sub>/Fe-based coatings were unchanged, but the intensity of the diffraction peaks of the CFe<sub>15.1</sub> phase decreased. When the content of CeO<sub>2</sub> was 1.5 wt%, the new phase of CeAl<sub>2</sub> appeared in the coating.
- (2) The addition of CeO<sub>2</sub> further reduced the size of the ceramic particles. With the increase in the CeO<sub>2</sub> content, the metal grain size reduced and then increased. MgAl<sub>2</sub>O<sub>4</sub>/Fe-based coatings with 1.0 wt% CeO<sub>2</sub> showed the finest metal grains.
- (3) The hardness of the MgAl<sub>2</sub>O<sub>4</sub>/Fe-based coatings increased, and the coefficient of friction and wear rate decreased with the increasing CeO<sub>2</sub> content. The sample with 1.0 wt% CeO<sub>2</sub> had a hardness of 856 HV<sub>10</sub> and a wear rate of  $3.84 \times 10^{-6} \text{ mm}^3 \cdot \text{N}^{-1} \cdot \text{m}^{-1}$ . Compared with the MgAl<sub>2</sub>O<sub>4</sub>/Fe-based coatings, the hardness increased by 10% and the wear rate was reduced by 40%, which could be attributed to metal grain refinement and dispersion strengthening. However, when the CeO<sub>2</sub> content was 1.5 wt%, the hardness of the MgAl<sub>2</sub>O<sub>4</sub>/Fe-based coatings decreased and the coefficient of friction and wear increased. It was attributed to the agglomeration of CeO<sub>2</sub>.

**Author Contributions:** Conceptualization, L.L. and S.S.; supervision, Y.L. and H.W.; writing—original draft, L.L.; writing—review and editing, S.S. and T.Z. All authors have read and agreed to the published version of the manuscript.

**Funding:** This research received no external funding.

**Institutional Review Board Statement:** Not applicable.

**Informed Consent Statement:** Not applicable.

**Data Availability Statement:** Data are contained within the article.

**Conflicts of Interest:** The authors declare no conflicts of interest.

## References

1. Ozkan, D. Structural characteristics and wear, oxidation, hot corrosion behaviors of HVOF sprayed  $\text{Cr}_3\text{C}_2\text{-NiCr}$  hardmetal coatings. *Surf. Coat. Technol.* **2023**, *457*, 129319. [[CrossRef](#)]
2. Guo, Y.Q.; Guo, L.; Liu, K.Y.; Qiu, S.Y.; Guo, H.B.; Xu, H.B. Mechanical properties and simulated thermal conductivity of biomimetic structured PS-PVD ( $\text{Gd}_{0.9}\text{Yb}_{0.1}$ ) $_2\text{Zr}_2\text{O}_7$  thermal barrier coatings. *J. Mater. Sci. Technol.* **2024**, *182*, 33–40. [[CrossRef](#)]
3. Yang, L.; Xiong, J.; Chen, X.X.; Li, X.R.; Deng, C.J.; Zhang, D.J.; Yi, L. Study on the growth and wear characters of CVD coating deposited on Ti(C, N)-based cermets with adding different C/N ratios of Ti(C, N) powders. *Ceram. Int.* **2023**, *49 Pt B*, 18023–18034. [[CrossRef](#)]
4. Liu, J.L.; Yu, H.J.; Chen, C.Z.; Weng, F.; Dai, J.J. Research and development status of laser cladding on magnesium alloys: A review. *Opt. Lasers Eng.* **2017**, *93*, 195–210. [[CrossRef](#)]
5. Zhuang, D.D.; Tao, W.W.; Zhang, Z.Y.; Du, B.; Zhang, S.H.; Lian, X.L.; Zhang, J.; Wang, D.; Feng, Y.J. Effects of ultrasound on the CrMnFeCoNi coatings with different TiC contents fabricated by laser cladding. *J. Alloys Compd.* **2023**, *960*, 170532. [[CrossRef](#)]
6. Wu, X.; Feng, S.K.; Zhang, W.G. Microstructure, phase composition and wear properties of iron-based gradient coatings by laser cladding on 65Mn steel. *Surf. Coat. Technol.* **2024**, *477*, 130290. [[CrossRef](#)]
7. Guo, W.M.; Li, X.Q.; Ding, N.; Liu, G.Q.; He, J.Q.; Tian, L.N.; Chen, L.Z.; Zairi, F. Microstructure characteristics and mechanical properties of a laser clad Fe-based martensitic stainless steel coating. *Surf. Coat. Technol.* **2021**, *408*, 126795. [[CrossRef](#)]
8. Duan, X.X.; Gao, S.Y.; Dong, Q.; Zhou, Y.F.; Xi, M.Z.; Xian, X.P.; Wang, B. Reinforcement mechanism and wear resistance of  $\text{Al}_2\text{O}_3/\text{Fe-Cr-Mo}$  steel composite coating produced by laser cladding. *Surf. Coat. Technol.* **2016**, *291*, 230–238. [[CrossRef](#)]
9. Liu, Y.; Gu, X.H.; Lou, C.H.; Kang, L. Influence of WC ceramic particles on structures and properties of laser cladding Ni50-WC coatings. *J. Mater. Res. Technol.* **2023**, *26*, 14–21. [[CrossRef](#)]
10. Yang, X.Y.; Wang, L.L.; Gao, Z.N.; Wang, Q.; Du, M.Z.; Zhan, X.H. WC distribution, microstructure evolution mechanism and microhardness of a developed Ti-6Al-4V/WC MMC coating fabricated by laser cladding. *Opt. Lasers Technol.* **2022**, *153*, 108232. [[CrossRef](#)]
11. Liu, D.J.; Hu, P.P.; Min, G.Q. Interfacial reaction in cast WC particulate reinforced titanium metal matrix composites coating produced by laser processing. *Opt. Lasers Technol.* **2015**, *69*, 180–186. [[CrossRef](#)]
12. Qi, C.Q.; Zhan, X.H.; Gao, Q.Y.; Liu, L.J.; Song, Y.Z.; Li, Y.P. The influence of the pre-placed powder layers on the morphology, microscopic characteristics and microhardness of Ti-6Al-4V/WC MMC coatings during laser cladding. *Opt. Lasers Technol.* **2019**, *119*, 105572. [[CrossRef](#)]
13. Zhang, H.; Pan, Y.J.; Zhang, Y.; Lian, G.F.; Cao, Q.; Que, L.Z. Microstructure, toughness, and tribological properties of laser clad  $\text{Mo}_2\text{FeB}_2$ -based composite coating with in situ synthesized WC and  $\text{La}_2\text{O}_3$  addition. *Surf. Coat. Technol.* **2022**, *449*, 128947. [[CrossRef](#)]
14. Chen, L.; Chen, W.G.; Li, D.Y.; Jing, P.Y.; Yin, H.Z.; Wu, H.J.; Xie, Y.; Wang, X.N. Effect of nano- $\text{La}_2\text{O}_3$  doping on the tribological behavior of laser clad WC-12Co coating on 65Mn steel under water lubrication condition. *Tribol. Int.* **2022**, *169*, 107428. [[CrossRef](#)]
15. Zhang, H.; Zou, Y.; Zou, Z.D.; Shi, C.W. Effects of  $\text{CeO}_2$  on microstructure and corrosion resistance of TiC-VC reinforced Fe-based laser cladding layers. *J. Rare Earths* **2014**, *32*, 1095–1100. [[CrossRef](#)]
16. Wang, H.Y.; Zuo, D.W.; Li, X.F.; Chen, K.M.; Huang, M.M. Effects of  $\text{CeO}_2$  nanoparticles on microstructure and properties of laser clad NiCoCrAlY coatings. *J. Rare Earths* **2010**, *28*, 246–250. [[CrossRef](#)]
17. Liu, L.C.; Wang, G.; Ren, K.; Di, Y.L.; Wang, L.P.; Rong, Y.; Wang, H.D. Marangoni flow patterns of molten pools in multi-pass laser cladding with added nano- $\text{CeO}_2$ . *Addit. Manuf.* **2022**, *59 Pt A*, 103156. [[CrossRef](#)]
18. Murmu, A.M.; Parida, S.K.; Das, A.K.; Kumar, S. Evaluation of laser cladding of Ti6Al4V-ZrO<sub>2</sub>-CeO<sub>2</sub> composite coating on Ti6Al4V alloy substrate. *Surf. Coat. Technol.* **2023**, *473*, 129988. [[CrossRef](#)]
19. Wei, C.; Wei, Y.S.; Wang, Z.J.; Chen, J.G. Improving Resistance to Crack and Corrosion of Laser-Clad TiC/Co-based Composite Coatings by Doping Minor CeO<sub>2</sub>. *Int. J. Electrochem. Sci.* **2022**, *17*, 220622. [[CrossRef](#)]
20. YZhao, H.; Sun, J.; Li, J.F. Effect of rare earth oxide on the properties of laser cladding layer and machining vibration suppressing in side milling. *Appl. Surf. Sci.* **2014**, *321*, 387–395.
21. Quazi, M.M.; Fazal, M.A.; Haseeb, A.S.M.A.; Yusof, F.; Masjuki, H.H.; Arslan, A. Effect of rare earth elements and their oxides on tribo-mechanical performance of laser claddings: A review. *J. Rare Earths* **2016**, *34*, 549–564. [[CrossRef](#)]
22. Sun, N.J.; Chen, Y.; Zhu, T.B.; Wang, H.; Pan, L.P.; Liao, N.; Li, Y.W.; Xie, Z.P. Tribological properties and wear resistance mechanism of WC-ZrO<sub>2</sub>-Al<sub>2</sub>O<sub>3</sub> ceramics. *J. Alloys Compd.* **2023**, *960*, 171069. [[CrossRef](#)]
23. Moon, J.; Lee, T.-H.; Kim, S.-D.; Lee, C.-H.; Jang, J.-H.; Shin, J.-H.; Lee, J.-W.; Lee, B.-H.; Suh, D.-W. Isothermal transformation of austenite to ferrite and precipitation behavior in 9Cr-1.5Mo-1.25Co-0.1C-VNb heat-resistant steel. *Mater. Charact.* **2020**, *170*, 110677. [[CrossRef](#)]
24. Han, G.Y.; Zhang, Y.F.; Wang, B.; Zhang, Z.X. Effect of the Addition of CeO<sub>2</sub> on the Microstructure and Corrosion of in-situ TiB/Ti Composite Coatings Prepared by Laser Cladding Technology. *Int. J. Electrochem. Sci.* **2021**, *16*, 210255. [[CrossRef](#)]

25. Liu, Y.N.; Sun, R.L.; Niu, W.; Zhang, T.G. Effects of CeO<sub>2</sub> on microstructure and properties of TiC/Ti<sub>2</sub>Ni reinforced Ti-based laser cladding composite coatings. *Opt. Lasers Eng.* **2019**, *120*, 84–94.
26. Wang, K.L.; Zhang, Q.B.; Sun, M.L.; Wei, X.G.; Zhu, Y.M. Microstructure and corrosion resistance of laser clad coatings with rare earth elements. *Corros. Sci.* **2001**, *43*, 255–267. [[CrossRef](#)]
27. Huang, Y.Z.; Ansari, M.; Asgari, H.; Farshidianfar, M.H.; Sarker, D.; Khamesee, M.B.; Toyserkani, E. Rapid prediction of real-time thermal characteristics, solidification parameters and microstructure in laser directed energy deposition (powder-fed additive manufacturing). *J. Mater. Process Technol.* **2019**, *274*, 116286. [[CrossRef](#)]
28. Zhao, S.B.; Jia, C.P.; Yuan, Y.X.; Wang, L.X.; Huang, Y.M.; Yang, L.J. Effects of laser remelting on microstructural characteristics of Ni-WC composite coatings produced by laser hot wire cladding. *J. Alloys Compd.* **2022**, *908*, 164612.
29. Ding, L.; Hu, S.S. Effect of nano-CeO<sub>2</sub> on microstructure and wear resistance of Co-based coatings. *Surf. Coat. Technol.* **2015**, *276*, 565–572. [[CrossRef](#)]
30. Zhang, L.S.; Zhang, M.; Zhu, Z.Y.; Gao, M.R.; Gao, J.; Guo, Z. Effects of nano-CeO<sub>2</sub> on microstructure and properties of Ni625 alloy prepared by laser cladding. *J. Alloys Compd.* **2022**, *918*, 165571. [[CrossRef](#)]
31. Gao, Z.T.; Ren, H.B.; Yuan, Y.; Gao, Z.M.; Liu, E.Y.; Zhang, C.W. Effect of CeO<sub>2</sub> on the microstructure and microhardness of laser-cladded Ni60 on 35CrMoV alloys. *Micron* **2021**, *150*, 103146. [[CrossRef](#)] [[PubMed](#)]
32. Zhao, T.; Cai, X.; Wang, S.X.; Shian, Z. Effect of CeO<sub>2</sub> on microstructure and corrosive wear behavior of laser-cladded Ni/WC coating. *Thin Solid Film.* **2000**, *379*, 128–132.
33. Shu, D.; Dai, S.C.; Wang, G.; Si, W.D.; Xiao, P.; Cui, X.X.; Chen, X. Influence of CeO<sub>2</sub> content on WC morphology and mechanical properties of WC/Ni matrix composites coating prepared by laser in-situ synthesis method. *J. Mater. Res. Technol.* **2020**, *9*, 11111–11120. [[CrossRef](#)]
34. Yan, M.W.; Li, Y.; Li, L.; Sun, Y.; Tong, S.H.; Sun, J.L. In-situ synthesis and reaction mechanism of MgAlON in Al<sub>2</sub>O<sub>3</sub>-MgO composites produced in flowing nitrogen. *Ceram. Int.* **2017**, *43*, 14791–14797. [[CrossRef](#)]
35. Yan, M.W.; Li, Y.; Li, H.Y.; Sun, Y.; Chen, H.Y.; Ma, C.H.; Sun, J.L. Evolution mechanism of MgAlON in the Al-Al<sub>2</sub>O<sub>3</sub>-MgO composite at 1800 °C in flowing nitrogen. *Ceram. Int.* **2018**, *44*, 3856–3861. [[CrossRef](#)]
36. Li, H.C.; Jiang, Z.Y.; Tieu, K.A.; Sun, W.H. Analysis of premature failure of work rolls in a cold strip plant. *Wear* **2007**, *263*, 1442–1446. [[CrossRef](#)]
37. Zhou, Y.; Wang, S.Q.; Huang, K.Z.; Zhang, B.; Wen, G.H.; Cui, X.H. Improvement of tribological performance of TC11 alloy via formation of a double-layer tribo-layer containing graphene/Fe<sub>2</sub>O<sub>3</sub> nanocomposite. *Tribol. Int.* **2017**, *109*, 485–495. [[CrossRef](#)]

**Disclaimer/Publisher’s Note:** The statements, opinions and data contained in all publications are solely those of the individual author(s) and contributor(s) and not of MDPI and/or the editor(s). MDPI and/or the editor(s) disclaim responsibility for any injury to people or property resulting from any ideas, methods, instructions or products referred to in the content.